A&A 436, 1123–1130 (2005)
DOI: 10.1051/0004-6361:20042025

Astronomy & Astrophysics

Atomic data from the Iron project

LVII. Radiative transition rates and collision strengths within the $3d^7$ configuration of Ni IV

M. Meléndez and M. A. Bautista

Centro de Física, Instituto Venezolano de Investigaciones Científicas (IVIC), PO Box 21827, Caracas 1020A, Venezuela
e-mail: [mmelende;mbautist]@ivic.ve

Received 17 September 2004 / Accepted 1 February 2005

Abstract. This paper reports on radiative transition rates and electron impact excitation rate coefficients for levels of the $3d^7$ ground configuration of Ni IV. The radiative data were computed using the Thomas-Fermi-Dirac central potential method, which allows for configuration interactions (CI) and relativistic effects in the Breit-Pauli formalism. Collision strengths in LS-coupling were calculated in the close coupling approximation with the R-matrix method. Then, fine structure collision strengths were obtained by means of the intermediate-coupling frame transformation (ICFT) method that accounts for spin-orbit coupling effects. The collision strengths were integrated over a Maxwellian distribution of electron energies, and the resulting effective collision strengths are given for a wide range of temperatures. We build a multilevel model for the Ni IV system and use it to identify the most important lines in optical and infrared spectra and to compute line ratios as diagnostics of nebular conditions. Finally, we test these data against recent observations of the bipolar planetary nebula Mz 3.

Key words. atomic data – atomic processes – line: formation – ISM: HII regions – ISM: planetary nebulae: general – ISM: planetary nebulae: individual: Mz 3

1. Introduction

Accurate atomic data for iron and other iron group elements is of major importance in astrophysics. Among these species, nickel is the second most abundant element; and under typical conditions of H II regions, Ni IV is the dominant ionization stage of that element. Ni IV is also important to the spectra of early supernova spectra.

The IRON Project is an international enterprise devoted to the computation of accurate atomic data for the iron group elements (Hummer et al. 1993). A complete list of publications from this project can be found at http://www.am.qub.uk/projects/iron/papers/. Within this project and following on previous efforts by A. Pradhan and his group at The Ohio State University, we have been systematically working on data for the low ionization stages of iron peak elements, e.g. radiative and collisional rates for Fe I–IV (Bautista & Pradhan 1998), Ni II (Bautista 1999, 2005), Ni III (Bautista 2001), and here we present a calculation for Ni IV. The first calculation of collisional data for Ni IV was presented by Sunderland et al. (2002), as a test case for a new parallel R-matrix program PRMAT. Nevertheless, this computation was wholly done in LS-coupling and is thus of limited practical use.

A recent spectroscopic study of the bipolar planetary nebula Mz 3 (Zhang & Liu 2002) found five Ni IV lines from forbidden transitions among levels of the $3d^7$ ground configuration, i.e. λ5041.6 ($^4F_{9/2}$–$^2G_{9/2}$), $\lambda\lambda$5289.4, 6126.3 ($^4F_{5/2}$–$^2G_{7/2}$ and $^4F_{5/2}$–$^4P_{3/2}$), and $\lambda\lambda$5363.4, 5904.0 ($^4F_{7/2}$–$^2G_{9/2}$ and $^4F_{7/2}$–$^4P_{5/2}$). In the present work, we build a multilevel model for the Ni IV ion, that can be used to analyze this and other nebulae. In this sense, we find that Ni IV emissivity line ratios are useful as diagnostics of electron densities between 10^6 and 10^8 cm^{-3}, where lines of iron ions and lighter species cannot be used.

2. Atomic data

2.1. Atomic structure calculations

We use the atomic structure code AUTOSTRUCTURE (Badnell 1986, 1997) based on the Thomas-Fermi-Dirac central potential to reproduce the structure of the Ni IV ion. This code is based on the program SUPERSTRUCTURE originally developed by Eissner et al. (1974). In this approach the wavefunctions are written as configuration interaction expansions of the type

$$\psi_i = \sum_j \phi_j c_{ji}, \tag{1}$$

where the coefficients c_{ji} are chosen so as to diagonalize $\langle\psi_i|H|\psi_i\rangle$. Here H is the Hamiltonian and the basic

Table 1. Spectroscopic and correlation configuration for Ni IV, and scaling parameters λ_{nl} for each spectroscopic orbital in the Thomas-Fermi-Dirac potential and the $4\bar{d}$ pseudo-orbital in the Coulomb potential.

	Configuration
Spectroscopic:	$3s^2 3p^6 3d^7$, $3s^2 3p^6 3d^6 4s$, $3s^2 3p^6 3d^6 4p$
Correlation:	$3s^2 3p^6 3d^5 4s^2$, $3s^2 3p^6 3d^5 4s4p$,
	$3s^2 3p^5 3d^8$, $3s^2 3p^5 3d^7 4s$, $3s^2 3p^5 3d^7 4p$
	$3s^2 3p^4 3d^9$, $3s3p^6 3d^8$, $3s3p^6 3d^7 4s$
	$3s3p^6 3d^7 4p$, $3p^6 3d^9$, $3p^6 3d^8 4s$
	$3p^6 3d^7 4s^2$, $3p^6 3d^7 4s4p$, $3p^6 3d^8 4p$
	$3s^2 3p^6 3d^6 4\bar{d}$
λ_{nl}	1s : 1.4301, 2s : 1.1423, 2p : 1.0864
	3s : 1.0704, 3p : 1.0601, 3d : 1.0282
	4s : 1.0330, 4p : 1.0541, $4\bar{d}$: –0.3969

functions ϕ_j are constructed from one-electron orbitals generated using the Thomas-Fermi-Dirac model potential (Eissner & Nussbaumer 1969). The λ_{nl} scaling parameters are optimized by minimizing a weighted sum of energies. The basic list of configurations and scaling parameters used in this work are listed in Table 1. The relatively large number of correlation configurations in our expansion was found to be important for an accurate representation of the target.

Relativistic effects are included in the calculation by means of the Breit-Pauli operators in the form:

$$H = H_{\rm nr} + H_{\rm bp}, \quad (2)$$

where $H_{\rm nr}$ is the usual non-relativistic Hamiltonian and $H_{\rm bp}$ the Breit-Pauli perturbation, which includes one- and two-body operators (see Jones 1970, 1971; Eissner et al. 1974). This Breit-Pauli perturbation is given by

$$H_{\rm bp} = H_{\rm 1b} + H_{\rm 2b} \quad (3)$$

where the one-body relativistic operators

$$H_{\rm 1b} = \sum_{n=1}^{N} f_n({\rm mass}) + f_n({\rm d}) + f_n({\rm so}) \quad (4)$$

represent the spin–orbit interaction f_n(so), and the non-fine structure mass-variation f_n(mass) and one-body Darwin f_n(d) corrections. The two-body corrections

$$H_{\rm 2b} = \sum_{n>m} g_{nm}({\rm so}) + g_{nm}({\rm ss}) + g_{nm}({\rm css}) + g_{nm}({\rm d}) + g_{nm}({\rm oo}), \quad (5)$$

usually referred to as the Breit interaction, include the fine structure terms g_{nm}(so) (spin–other-orbit and mutual spin–orbit) and g_{nm}(ss) (spin–spin), and the non-fine structure terms g_{nm}(css) (spin–spin contact), g_{nm}(d) (Darwin), and g_{nm}(oo) (orbit–orbit).

The expansion considered here for the Ni IV system includes 36 LS terms. Table 2 presents the complete list of states included, as well as a comparison between the calculated target term energies and the observed energies taken from NIST (2000), averaged over fine structure. Here we show the LS-coupling energies without relativistic effects and those that allow for one- and two-body relativistic corrections. We find that the 2-body relativistic operators have only negligible

Table 2. Calculated and observed term energies (in Ryd) for Ni IV. The second column shows the ab initio energies neglecting relativistic effects (no relat.); the third column shows the energies including the effects of mass, velocity, and Darwin relativistic effects (1-B relat.) but without two-body interactions; the fourth column gives the calculated energies allowing for all relativistic effects (2-B rel.); and the fifth column gives the experimental energies from NIST (2000).

Level	Present			Experiment
	No relat.	1-B rel.	2-B rel.	NIST (2000)
$3d^7\ ^4F$	0.000000	0.000000	0.000000	0.00000
$3d^7\ ^4P$	0.167744	0.168143	0.167232	0.15664
$3d^7\ ^2G$	0.194507	0.194612	0.194259	0.17473
$3d^7\ ^2P$	0.213619	0.214542	0.215411	0.20805
$3d^7\ ^2H$	0.273222	0.273044	0.273261	0.23661
$3d^7\ ^2D$	0.244796	0.245531	0.248822	0.24255
$3d^7\ ^2F$	0.426665	0.427212	0.427617	0.38753
$3d^7\ ^2D$	0.642415	0.643563	0.645014	0.60678
$3d^6 4s\ ^6D$	1.050524	1.021174	1.021967	1.00332
$3d^6 4s\ ^4D$	1.174054	1.144630	1.145408	1.09810
$3d^6 4s\ ^4P$	1.329187	1.300472	1.301645	1.26161
$3d^6 4s\ ^4H$	1.323730	1.294378	1.293635	1.26227
$3d^6 4s\ ^4F$	1.348514	1.319496	1.319164	1.27956
$3d^6 4s\ ^4G$	1.385653	1.356394	1.357487	1.31596
$3d^6 4s\ ^2P$	1.401766	1.373031	1.375162	1.31259
$3d^6 4s\ ^2H$	1.396225	1.366841	1.367147	1.32057
$3d^6 4s\ ^2F$	1.422926	1.393841	1.393851	1.33768
$3d^6 4s\ ^2G$	1.458127	1.428833	1.430886	1.37387
$3d^6 4s\ ^4D$	1.471055	1.441942	1.442994	1.38750
$3d^6 4s\ ^2I$	1.474509	1.445083	1.445357	1.40451
$3d^6 4s\ ^2G$	1.490605	1.461311	1.464264	1.41399
$3d^6 4s\ ^2D$	1.546979	1.517824	1.517252	1.44471
$3d^6 4s\ ^2S$	1.554798	1.525544	1.528841	
$3d^6 4s\ ^2D$	1.552943	1.524521	1.528960	
$3d^6 4s\ ^2F$	1.647569	1.618736	1.619422	1.55148
$3d^6 4p\ ^6D^o$	1.612450	1.600081	1.599185	1.59328
$3d^6 4s\ ^4F$	1.736458	1.707397	1.709217	1.62704
$3d^6 4p\ ^6F^o$	1.682306	1.669815	1.669569	1.64876
$3d^6 4p\ ^6P^o$	1.709164	1.696714	1.696861	1.67615
$3d^6 4p\ ^4D^o$	1.736066	1.723675	1.725165	1.68833
$3d^6 4s\ ^2F$	1.812385	1.783258	1.784634	1.68428
$3d^6 4p\ ^4F^o$	1.750378	1.737852	1.738949	1.69828
$3d^6 4s\ ^4P$	1.734944	1.706121	1.707983	
$3d^6 4p\ ^4P^o$	1.791677	1.779220	1.779713	1.73270
$3d^6 4s\ ^2G$	1.843564	1.814675	1.816295	1.72906
$3d^6 4s\ ^2P$	1.812817	1.783908	1.786087	

effects, less than 0.1%, on the averaged term energies. Mass, velocity, and Darwin operators, on the other hand, lower the computed energies between 1% and 2% for the $3d^6 4s$ and $3d^6 4p$ terms to bring them closer to experimental values. In our best target representation, the theoretical energies for the lowest eight terms are typically within 5% of the experimental values, and for the higher terms the agreement is within 2%.

For calculating radiative rates, fine tuning is performed with term energy corrections, where the improved relativistic wavefunction $\psi_i^{\rm R}$ is obtained in terms of the non-relativistic functions

$$\psi_i^{\rm R} = \psi_i^{\rm LS} + \sum_{j\neq i} \psi_j^{\rm LS} \times \frac{\langle \psi_j^{\rm LS} | H_{\rm bp} | \psi_i^{\rm LS} \rangle}{E_i^{\rm LS} - E_j^{\rm LS}}, \quad (6)$$

with the LS energy differences $E_i(\mathrm{LS}) - E_j(\mathrm{LS})$ adjusted to fit weighted averaged energies of the experimental multiplets (Zeippen et al. 1977). The effects of TECs and relativistic operators on the fine structure levels are illustrated in Table 3 for the first six $3d^7$ multiplets of the Ni IV ion.

For dipole allowed transitions, spontaneous decay rates are given by

$$A_{ij}(E1) = 2.6774 \times 10^9 (E_i - E_j)^3 \frac{1}{g_i} S_{ij}^{E1} \ \ (s^{-1}), \quad (7)$$

while for forbidden transitions we consider electric quadrupole ($E2$) and magnetic dipole ($M1$) transition rates given by

$$A_{ij}(E2) = 2.6733 \times 10^3 (E_i - E_j)^5 \frac{1}{g_i} S_{ij}^{E2} \ \ (s^{-1}) \quad (8)$$

$$A_{ij}(M1) = 3.5644 \times 10^4 (E_i - E_j)^3 \frac{1}{g_i} S_{ij}^{M1} \ \ (s^{-1}), \quad (9)$$

where g_i is the statistical weight of the upper initial level i, S_{ij} the line strength, and E the energy in Rydberg.

Equations (7)–(9) show that the transition rates are sensitive to the energy levels accuracy, particularly for forbidden transitions between levels with small energy difference. Thus, we perform further adjustments to the transitions rates by correcting out best calculated energies to experimental values. Such corrections are called "Level Energy Corrections (LECs)".

In Fig. 1 we plot the gf-values for dipole allowed transitions among fine structure levels computed in the length gauge vs. those in the velocity gauge. The overall agreement between the two gauges is around 20% for $\log(gf)$-values greater than -3, which offers a good indicator of the quality of the dipole allowed radiative data.

As regards forbidden transitions, Tables 4 and 5 present transition probabilities for magnetic dipole and electric quadrupole transitions rates for the ^{4}F, ^{4}P, ^{2}G, and ^{2}P levels within the $3d^7$ ground configuration of Ni IV. Here we show the effects of TECs and 2-body relativistic operators on the radiative rates for forbidden transitions. These effects go from a few percent in most cases to several factors for some transitions that involve highly mixed levels. We also compare the present data with those by Hansen et al. (1984) and Garstang (1968), who used the method of parametric fitting to observed energy level structure. Overall, there is good agreement between our best results (TEC + 2-body) and the data of these authors, except for a few weak transitions. From these comparisons, the observed accuracy in the representation of the energy level structure of the ions and analysis of the completeness of the configurations expansion used in the calculation we estimate that the transition rates for forbidden transitions among lowly excited levels have an accuracy of ∼20%.

Table 3. Calculated and observed fine structure energy levels. (a) With neither 2-body relativistic operators nor TECs; (b) including 2-body relativistic effects, but without TECs; (c) with 2-body relativistic operators and TECs.

Level	Present			Experiment
	(a)	(b)	(c)	
$4F_{9/2}$	0.000000	0.000000	0.000000	0.000000
$4F_{7/2}$	0.011524	0.010965	0.011006	0.010841
$4F_{5/2}$	0.019826	0.018864	0.018908	0.018613
$4F_{3/2}$	0.025453	0.024230	0.024266	0.023885
$4P_{5/2}$	0.175599	0.175910	0.165389	0.165109
$4P_{3/2}$	0.177558	0.177976	0.167690	0.167371
$4P_{1/2}$	0.184077	0.183526	0.173089	0.172762
$2G_{9/2}$	0.201011	0.200450	0.180734	0.180701
$2G_{7/2}$	0.211793	0.210452	0.190982	0.190889
$2P_{3/2}$	0.222958	0.223050	0.215622	0.215505
$2P_{1/2}$	0.233077	0.232044	0.224644	0.224640
$2H_{11/2}$	0.281112	0.279733	0.243154	0.242844
$2H_{9/2}$	0.290788	0.288895	0.252627	0.252217
$2D_{5/2}$	0.253152	0.253031	0.246800	0.246921
$2D_{3/2}$	0.271001	0.269100	0.262786	0.262242

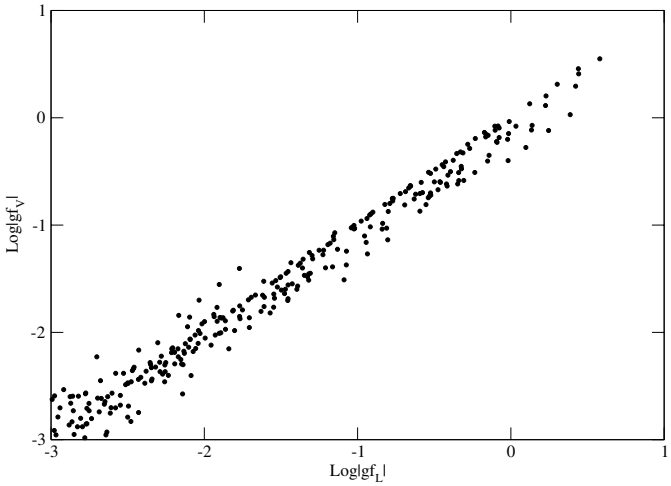

Fig. 1. Log $gf_{\rm V}$ plotted against Log $gf_{\rm L}$ for transitions between calculated energy levels.

Table 4. Magnetic dipole transition rates (in s^{-1}) for levels within $3d^7$ ground state configuration of Ni IV. The table shows results computed with neither TEC nor 2-body relativistic operators (w/o T + w/o 2-body), with 2-body relativistic operators (w/o T + 2-body), with TECs and 2-body relativistic operators (T + 2-body) and with TECs, LEVs and 2-body relativistic operators (T + L + 2-body). The rates previously reported by Hansen et al. (1984) and Garstang (1969) are also given.

		$A_{ij}(M1)$					
Term i	Term j	w/o T +w/o 2-body	w/o T + 2-body	T + 2-body	T + L + 2-body	Hansen	Garstang
$^4F_{7/2}$	$^4F_{9/2}$	6.80E−2	5.87E−2	5.94E−2	5.67E−2	5.70E−2	4.80E−2
$^4F_{5/2}$	$^4F_{7/2}$	4.36E−2	3.76E−2	3.76E−2	3.58E−2	3.60E−2	3.20E−2
$^4F_{3/2}$	$^4F_{5/2}$	1.52E−2	1.32E−2	1.31E−2	1.25E−2	1.30E−2	1.10E−2
$^4P_{5/2}$	$^4F_{7/2}$	1.03E−2	8.55E−3	7.38E−3	7.36E−3	5.30E−3	4.70E−3
$^4P_{5/2}$	$^4F_{5/2}$	3.49E−3	2.75E−3	2.53E−3	2.53E−3	2.00E−3	1.70E−3
$^4P_{5/2}$	$^4F_{3/2}$	1.25E−3	1.00E−3	9.18E−4	9.20E−4	6.90E−4	6.10E−4
$^4P_{3/2}$	$^4F_{5/2}$	3.47E−3	2.01E−3	1.55E−3	1.55E−3	1.80E−3	1.00E−3
$^4P_{3/2}$	$^4F_{3/2}$	7.92E−4	3.42E−4	1.88E−4	1.88E−4	3.30E−4	9.00E−5
$^4P_{3/2}$	$^4P_{5/2}$	2.16E−4	2.58E−4	3.61E−4	3.43E−4	3.40E−4	7.30E−4
$^4P_{1/2}$	$^4F_{3/2}$	7.16E−7	5.06E−6	7.54E−6	7.55E−6	1.50E−6	7.90E−6
$^4P_{1/2}$	$^4P_{3/2}$	1.55E−2	9.67E−3	8.96E−3	8.92E−3	8.90E−3	8.00E−3
$^2G_{9/2}$	$^4F_{9/2}$	1.18E+0	9.39E−1	8.44E−1	8.43E−1	9.10E−1	8.30E−1
$^2G_{9/2}$	$^4F_{7/2}$	3.62E−1	3.00E−1	2.64E−1	2.64E−1	2.80E−1	2.60E−1
$^2G_{7/2}$	$^4F_{9/2}$	4.35E−2	3.57E−2	3.29E−2	3.29E−2	3.40E−2	3.10E−2
$^2G_{7/2}$	$^4F_{7/2}$	4.52E−1	3.53E−1	3.17E−1	3.18E−1	3.50E−1	3.20E−1
$^2G_{7/2}$	$^4F_{5/2}$	3.31E−1	2.64E−1	2.34E−1	2.35E−1	2.50E−1	2.40E−1
$^2G_{7/2}$	$^2G_{9/2}$	2.44E−2	1.95E−2	2.09E−2	2.05E−2	2.00E−2	1.80E−2
$^2P_{3/2}$	$^4F_{5/2}$	2.46E−1	1.90E−1	1.76E−1	1.76E−1	1.70E−1	2.30E+1
$^2P_{3/2}$	$^4F_{3/2}$	1.76E−1	1.34E−1	1.25E−1	1.26E−1	1.20E−1	1.60E−1
$^2P_{3/2}$	$^4P_{5/2}$	3.51E−1	2.89E−1	3.08E−1	3.11E−1	3.30E−1	3.20E+1
$^2P_{3/2}$	$^4P_{3/2}$	1.79E−1	1.47E−1	1.56E−1	1.58E−1	1.70E−1	1.60E+1
$^2P_{3/2}$	$^4P_{1/2}$	6.10E−2	5.39E−2	5.91E−2	5.99E−2	6.40E−2	6.00E−2
$^2P_{1/2}$	$^4F_{3/2}$	5.40E−3	3.10E−3	3.21E−3	3.23E−3	3.90E−3	3.50E−3
$^2P_{1/2}$	$^4P_{3/2}$	9.66E−4	7.42E−4	6.97E−4	7.08E−4	6.40E−4	5.00E−4
$^2P_{1/2}$	$^4P_{1/2}$	4.46E−1	3.61E−1	3.84E−1	3.91E−1	4.20E−1	4.20E+1
$^2P_{1/2}$	$^2P_{3/2}$	2.30E−2	1.63E−2	1.65E−2	1.71E−2	1.70E−2	2.30E−2

2.2. Scattering calculations

In the close coupling (CC) approximation the total wave function of the electron-ion system is represented as

$$\psi(E;\mathrm{LS}\pi) = A\sum_i \chi_i\theta_i + \sum_j c_j\Phi_j, \tag{10}$$

where χ_i is the target ion wave function in a specific state $S_i\,L_i$, θ_i is wave function of the free electron, Φ_j short range correlation functions for the bound (e+ion) system, and A the antisymetrization operator.

The variational procedure gives rise to a set of coupled integro-differential equations that are solved by the R-matrix technique (Burke et al. 1971; Berrington 1978, 1995) within a box of radios $r \le a$. In the asymptotic region $r > a$ exchange between the outer electron and the target ion can be neglected and if all long-range potentials beyond Coulombic are also neglected, the reactance K-matrix and the scattering S-matrix are obtained by matching the inner-radial functions at the boundary to linear combinations of the outer-region Coulomb solutions. Later, contributions of long-range potentials to the collision strengths are included perturbatively (see Griffin et al. 1999).

The S-matrix elements determine collision strength for a transition from an initial target state i to a final target state f

$$\Omega_{if} = \frac{1}{2}\sum w|S_{if} - \delta_{if}|, \tag{11}$$

where $w = (2L+1)(2S+1)$ or $(2J+1)$ depending on the coupling scheme, and the summation runs over the partial waves and channels coupling the initial and final state of interest.

To calculate collision strengths we used the same basic expansion shown in Tables 1 and 2. Since our R-matrix

Table 5. Electric quadrupole transition rates (in s^{-1}) for levels within the $3d^7$ ground state configuration of Ni IV. The table shows the results computed with neither TEC nor 2-body relativistic operators (w/o T + w/o 2-body), with 2-body relativistic operators (w/o T + 2-body), with TECs and 2-body relativistic operators (T + 2-body) and with TECs, LEVs and 2-body relativistic operators (T + L + 2-body). The rates previously reported by Hansen et al. (1984) and Garstang (1969) are also given.

		$A_{ij}(E2)$					
Term i	Term j	w/o T + w/o 2-body	w/o T + 2-body	T + 2-body	T + L + 2-body	Hansen	Garstang
$^4F_{7/2}$	$^4F_{9/2}$	5.65E−09	4.41E−09	4.49E−09	4.16E−09	3.40E−09	2.50E−09
$^4F_{5/2}$	$^4F_{7/2}$	1.61E−09	1.25E−09	1.25E−09	1.15E−09	9.40E−10	7.40E−10
$^4F_{3/2}$	$^4F_{5/2}$	2.67E−10	2.11E−10	2.09E−10	1.93E−10	1.60E−10	1.20E−10
$^4P_{5/2}$	$^4F_{9/2}$	1.16E−01	1.18E−01	8.65E−02	8.57E−02	6.80E−02	6.20E−02
$^4P_{5/2}$	$^4F_{7/2}$	2.66E−02	2.74E−02	1.97E−02	1.96E−02	1.50E−02	1.50E−02
$^4P_{5/2}$	$^4F_{5/2}$	4.57E−03	4.76E−03	3.36E−03	3.36E−03	2.70E−03	2.50E−03
$^4P_{5/2}$	$^4F_{3/2}$	4.23E−04	4.44E−04	3.09E−04	3.11E−04	2.50E−04	2.40E−04
$^4P_{3/2}$	$^4F_{7/2}$	5.78E−02	6.05E−02	4.44E−02	4.42E−02	3.50E−02	3.40E−02
$^4P_{3/2}$	$^4F_{5/2}$	3.28E−02	3.47E−02	2.50E−02	2.50E−02	2.00E−02	1.90E−02
$^4P_{3/2}$	$^4F_{3/2}$	9.08E−03	9.67E−03	6.89E−03	6.91E−03	5.40E−03	5.40E−03
$^4P_{3/2}$	$^4P_{5/2}$	1.51E−11	1.99E−11	3.42E−11	3.14E−11	2.40E−11	8.10E−11
$^4P_{1/2}$	$^4F_{5/2}$	4.45E−02	4.54E−02	3.28E−02	3.28E−02	2.60E−02	2.50E−02
$^4P_{1/2}$	$^4F_{3/2}$	5.79E−02	5.93E−02	4.23E−02	4.24E−02	3.30E−02	3.20E−02
$^4P_{1/2}$	$^4P_{3/2}$	9.97E−10	4.49E−10	3.92E−10	3.89E−10	3.00E−10	2.40E−10
$^2G_{9/2}$	$^4F_{9/2}$	2.47E−04	1.97E−04	1.43E−04	1.42E−04	1.30E−04	1.20E−04
$^2G_{9/2}$	$^4F_{7/2}$	1.12E−05	9.16E−06	7.06E−06	7.09E−06	6.60E−06	5.70E−06
$^2G_{9/2}$	$^4F_{5/2}$	1.98E−05	1.56E−05	9.65E−06	9.73E−06	8.90E−06	7.70E−06
$^2G_{7/2}$	$^4F_{9/2}$	4.30E−05	3.23E−05	2.53E−05	2.52E−05	2.40E−05	2.00E−05
$^2G_{7/2}$	$^4F_{7/2}$	5.42E−05	4.21E−05	3.07E−05	3.07E−05	2.90E−05	2.60E−05
$^2G_{7/2}$	$^4F_{5/2}$	5.30E−06	4.35E−06	2.83E−06	2.84E−06	2.60E−06	2.30E−06
$^2G_{7/2}$	$^4F_{3/2}$	3.32E−05	2.70E−05	1.62E−05	1.64E−05	1.60E−05	1.30E−05
$^2G_{7/2}$	$^2G_{9/2}$	2.05E−09	1.29E−09	1.72E−09	1.67E−09	1.60E−09	1.20E−09
$^2P_{3/2}$	$^4F_{7/2}$	1.89E−02	1.61E−02	1.18E−02	1.18E−02	9.90E−03	7.20E−03
$^2P_{3/2}$	$^4F_{5/2}$	8.24E−03	7.11E−03	5.01E−03	5.03E−03	4.30E−03	2.90E−03
$^2P_{3/2}$	$^4F_{3/2}$	2.00E−03	1.73E−03	1.19E−03	1.20E−03	1.10E−03	7.40E−04
$^2P_{3/2}$	$^4P_{5/2}$	6.73E−06	5.56E−06	6.58E−06	6.68E−06	5.80E−06	5.60E−06
$^2P_{3/2}$	$^4P_{3/2}$	3.88E−06	3.06E−06	3.56E−06	3.63E−06	2.60E−06	2.90E−06
$^2P_{3/2}$	$^4P_{1/2}$	5.45E−08	5.23E−08	7.48E−08	7.66E−08	4.40E−08	5.60E−08
$^2P_{1/2}$	$^4F_{5/2}$	8.20E−03	6.78E−03	5.10E−03	5.14E−03	4.20E−03	3.40E−03
$^2P_{1/2}$	$^4F_{3/2}$	4.65E−03	3.89E−03	2.68E−03	2.70E−03	2.40E−03	1.70E−03
$^2P_{1/2}$	$^4P_{5/2}$	1.07E−05	7.94E−06	9.01E−06	9.21E−06	8.00E−06	8.40E−06
$^2P_{1/2}$	$^4P_{3/2}$	3.43E−07	2.14E−07	2.04E−07	2.10E−07	4.30E−07	3.90E−07
$^2P_{1/2}$	$^2P_{3/2}$	1.64E−08	8.66E−09	8.65E−09	9.20E−09	8.10E−09	1.50E−08

calculations only include the one-body relativistic operators, the third column of Table 2 best represents the quality of the target for the present collisional calculations. One problem with the current target can be seing in the predicted relative order of the terms $3d^7$ ^2D and ^2H. These two states are difficult to represent because they are mixed at the fine structure level. In theory, one should be very careful computing collision strengths among states whose relative energy order is incorrect because spin-orbit coupling of fine structure levels may affect the resonance structures. However, in the present case we do not expect to find major errors due to reversed order of these terms, because the J values of the associated levels are all very different and not coupled to each other.

Collision strengths and effective collision strengths were calculated for all transitions between the lowest 8 even parity terms that yield 19 levels. The additional higher excitation terms shown in Table 2 were also included in the CC calculation, yet the collision strengths involving these terms may be inaccurate due to the lack of correlation interaction. In the case of the $3d^64p$ configuration there are also problems because of the incomplete list of levels included, thus there maybe collisional coupling effects that are unaccounted for. The importance

Table 6. Comparison between the present effective collision strengths in LS-coupling and those of Sunderland et al. (2002). The data is for transitions from the $3d^7\ ^4F$ ground state to other terms of the $3d^7$ configuration.

	5000 K		10 000 K		40 000 K	
	Present	Sunderland	Present	Sunderland	Present	Sunderland
^4P	7.337	6.851	7.050	6.049	5.322	4.527
^2G	3.260	2.959	3.259	2.857	3.378	2.876
^2P	1.018	1.121	1.035	0.9661	1.063	0.8726
^2H	2.997	2.360	3.040	2.632	3.442	1.969
^2D	2.021	1.201	1.838	1.274	1.746	1.369
^2F	1.764	1.451	1.961	1.536	1.842	1.467
$^2D2$	0.637	0.6145	0.697	0.6437	0.7909	0.7117

of including a large CC expansion, beyond the terms of the $3d^7$ configuration, was demonstrated by Sunderland et al. (2002). They showed that the collision strengths for transitions within the $3d^7$ configuration were underestimated by up to 40% when the calculation neglected states of the $3d^6$ 4s and $3d^6$ 4p.

The computations were carried out with the RMATRX package of codes (Berrington 1995). The set of (N+1)-electron wavefunctions on the right hand of the CC expansion in Eq. (10) includes all the configurations that result from adding an additional electron to the target configurations. Partial wave contributions are include from 104 $SL\pi$ total symmetries with angular momentum $L = 0{-}12$, total multiplicities $(2S + 1) = 1{-}7$, and parities even and odd. Additional contributions from partial waves up to $L = 60$ were computed without exchange, which is a good approximation for high partial waves. Beyond this point the collision strengths were "topped up" with estimates of high partial waves contributions based on the Coulomb-Bethe approximation (Burgess 1974). For all transitions the contributions from the high partial waves is less than 20%. The collision strengths were calculated at 22 000 energy points from 0 to 12 Ry, with a resolution of 10^{-5} Ry in the region with resonances and 5×10^{-3} Ry at higher energies. This resolution was found sufficient for accurate calculations of effective collision strengths.

A dimensionless thermally-averaged effective collision strength results from averaging the collision strength over a Maxwellian distribution for electron velocities

$$\Upsilon_{if} = \int_0^\infty \Omega_{if} \exp(-\epsilon_f/kT)\mathrm{d}(\epsilon_f/kT), \qquad (12)$$

where ϵ_f is the kinetic energy of the outgoing electron, T the electron temperature in Kelvin and $k = 6.339 \times 10^{-6}$ Ry/K is the Boltzmann's constant. For the present work we have computed effective collision strengths for various temperatures that expand from 5000 K to 180 000 K. This range covers the regimens of both photoionized and coronal plasmas.

In Table 6 we compare the present LS effective collision strengths with those of Sunderland et al. (2002). Agreement between the two sets of data is good (within ∼20%), with the exception of the effective collision strengths for the $^4F{-}^2D$ transition, which differs by ∼40%. The reasons for discrepancy seem related to the difference in the target representations. Our target representation yields reasonably accurate energies, but the ^2H and ^2D terms come out in reverse energy order. By contrast, the target representation of Sunderland et al. (2002) does predict the ^2H and ^2D terms in the correct order; yet their computed energies are considerably overestimated for all states of the $3d^7$ configuration, perhaps due to missing configuration interaction.

In order to investigate differences between the present results and those of Sunderland et al. (2002), we carried out additional calculations with reduced configuration expansions. Here we tried to remove all configurations with two-electron jumps from the 3s and 3p orbitals from the CC expansion, but without major detriment to the target. Thus we worked with two new configuration expansions: (a) a 10-configuration expansion that includes the correlation configurations $3s^23p^53d^8$, $3s^23p^53d^74s$, $3s^23p^43d^9$, $3s3p^63d^8$, $3s3p^63d^74s$, $3s3p^63d^74p$, and $3s^23p^63d^64\bar{d}$; (b) a 12-configuration expansion that includes $3s^23p^53d^74p$ and $3s^23p^63d^54s4p$ in addition to the configurations in (a). In all calculations we maintained the same number of LS terms in the CC expansion. Table 6 shows a comparison between effective collision strengths obtained from our calculations and the results of Sunderland et al. (2002). This table offers a good explanation for the discrepancies between our results and those of Sunderland et al. One can see that the collision strengths vary by up to 20% between our various calculations. In particular, we find that the collision strength for the $^4F{-}^2D$ transition obtained from the 10-configuration expansion is only ∼20% higher than that of Sunderland et al. (2002), yet this collision strength grows with the number of configurations in the target representation.

Collision strengths for the fine-structure levels were obtained by re-coupling unphysical LS reactance matrices and then converting them to the physical matrices by means of multi-channel quantum defect theory. This is the so-called intermediate-coupling frame transformation (ICFT) method of Griffin et al. (1998), which accounts for the spin-orbit effects that are very important for the Ni IV system. Hence, we find differences of up to several factors between the ICFT results and fine structure collision strengths obtained from algebraic recoupling that reach up to several factors for many transitions.

Figure 2 shows the collision strength for a sample of transitions between levels of the lowest four multiplets. Consequently, Fig. 3 shows the effective collision strength for the same transitions over a wide range of temperatures.

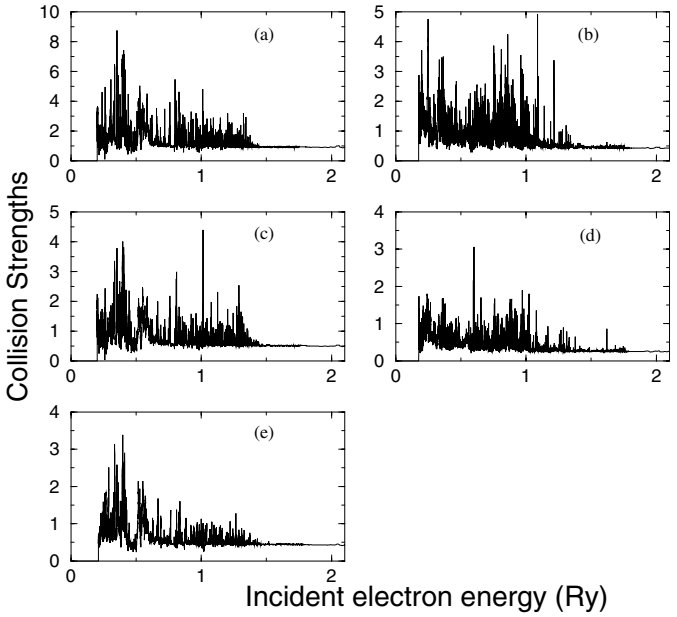

Fig. 2. Collision strengths for the Ni IV ion for transitions within the $3d^7$ configuration: **a)** $^4F_{9/2}$–$^2G_{9/2}$; **b)** $^4F_{5/2}$–$^2G_{7/2}$; **c)** $^4F_{7/2}$–$^2G_{9/2}$; **d)** $^4F_{7/2}$–$^4P_{5/2}$; **e)** $^4F_{5/2}$–$^4P_{3/2}$.

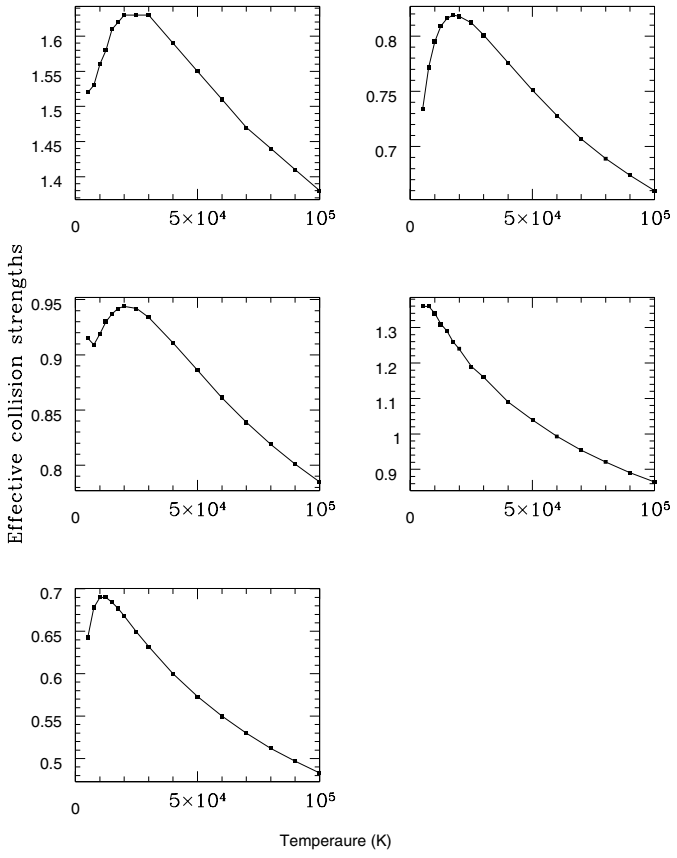

Fig. 3. Effective collision strengths for the Ni IV ion for the same transitions as in Fig. 2.

3. The Ni IV emission spectra

We build a collisional-radiative model of the Ni IV ion using the data described above. This model is used to study the emission spectrum of the system, identifying the most important lines and selecting line emissivity ratios useful as diagnostics of physical conditions in non-LTE plasmas.

For typical nebular temperatures between 7000 and 15 000 K, the strongest lines appear in the optical region. For electron densities $<10^6$ cm^{-1} the dominant lines are λ5517.66 ($a\ ^4F_{9/2}$–$a\ ^4P_{5/2}$) and λ5041.56 ($a\ ^4F_{9/2}$–$a\ ^2G_{9/2}$), but even these are rather weak. Higher densities favor the appearance of several other lines and the likelihood that the Ni IV spectrum can be observed. In this case, the strongest lines are λ5041.56 ($a\ ^4F_{9/2}$–$a\ ^2G_{9/2}$), λ5363.30 ($a\ ^4F_{3/2}$–$a\ ^2G_{9/2}$), and λ5288.22 ($a\ ^4F_{5/2}$–$a\ ^2G_{7/2}$). These lines were all identified in the spectrum of the bipolar planetary nebula Mz 3 (Zhang & Liu 2002) together with the transitions λ5517.66 ($a\ ^4F_{7/2}$–$a\ ^4P_{5/2}$) and λ6124.10 ($a\ ^4F_{3/2}$–$a\ ^4P_{1/2}$).

Figure 4 depicts the line emissivity ratios $j(\lambda5041)/j(\lambda5903)$ and $j(\lambda5363)/j(\lambda5903)$ vs. the logarithm of the electron density for various temperatures. These line ratios are

Table 7. Comparison between the effective collision strengths at 10 000 K in LS-coupling obtained from three different configuration expansions for the target and those of Sunderland et al. (2002). The data is for transitions from the $3d^7\ ^4F$ ground state to other terms of the $3d^7$ configuration.

	10-conf	12-conf	18-conf	Sunderland
^{4}P	6.916	7.358	7.050	6.049
^{2}G	3.393	3.514	3.259	2.857
^{2}P	1.028	1.132	1.035	0.966
^{2}H	3.316	3.164	3.040	2.632
^{2}D	1.596	1.762	1.838	1.274
^{2}F	1.828	1.922	1.961	1.536
^{2}D2	0.725	0.729	0.697	0.644

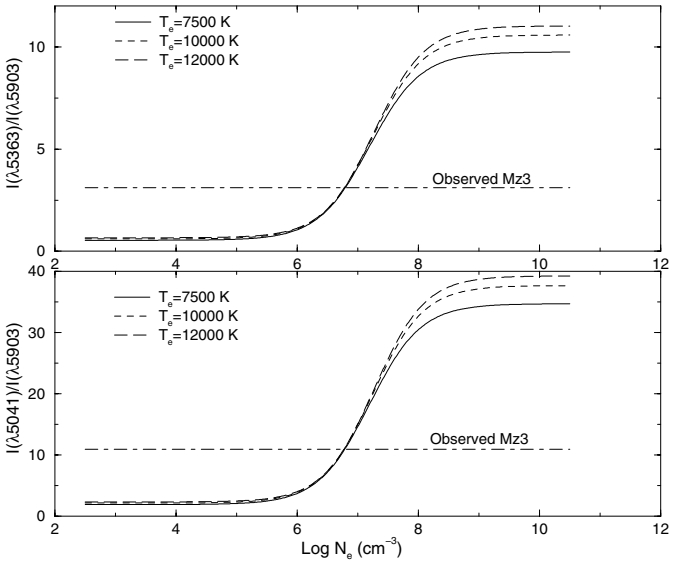

Fig. 4. Emissivity line ratios vs. Log N_e for various temperatures. The horizontal lines indicate the observed ratios in the spectra of Mz 3 (Zhang & Liu 2002).

sensitive to electron density in the Log $N_e(cm^{-3})$ range from 6 to 8. The plots also show line ratios observed in the spectra of Mz 3 (Zhang & Liu 2002), which indicate electron density log $N_e(cm^{-3}) \approx 6.6$. This diagnostic agrees very closely with the density derived from [FeIII] lines.

4. Conclusions

We have computed radiative data, collision strengths, and effective collision strengths for transitions among 19 levels from the $3d^7$ ground configuration of Ni IV. The radiative data were calculated using the Thomas-Fermi-Dirac central potential and the rates for dipole forbidden transitions were found in good agreement with previous semi-empirical calculations by Hansen et al. (1984) and Garstang (1968). The collisional data for Ni IV obtained from the R-matrix method is presented for the first time. These collision strengths account for relativistic effects and contributions from extensive resonance structures.

The complete set of data obtained here allows us to build a non-LTE collisional-radiative model for Ni IV, which was then used to study the Ni IV emission from typical photoionized nebulae. Furthermore, we demonstrate the usefulness of various Ni IV emissivity line ratios as diagnostics of electron density between 10^6 and 10^8 cm^{-3}, beyond the range of sensitivity of line ratios from iron ions and lighter species.

The whole set of data reported here can be obtained in electronic form from the CDS or by request to the authors.

Acknowledgements. We are grateful to N.R. Badnell, K. Butler, and W. Eissner for comments and corrections that led to substantial improvement of the manuscript.

References

Badnell, N. R. 1986, J. Phys. B: At. Mol. Opt. Phys., 19, 3827
Badnell, N. R. 1997, J. Phys. B: At. Mol. Opt. Phys., 30, 1
Bautista, M. A., & Pradhan 1998, Rev. Mex. Astron. Astrofis, 7, 163
Bautista, M. A. 1999, A&AS, 137, 529
Bautista, M. A. 2001, A&A, 365, 268
Bautista, M. A. 2005, A&A, in press
Berrington, K. A., Burke, P. G., Chang, J. J., et al. 1974, Comput. Phys. Commun., 8, 149
Berrington, K. A., Burke, P. G., Le Dourneuf, M., et al. 1978, Comput. Phys. Commun., 14, 367
Berrington, K. A., Eissner, W., & Norrington, P. H. 1995, Comput. Phys. Commun., 92, 290
Burgess, A. 1974, J. Phys. B: At. Mol. Opt. Phys., 7, L364
Burke, V. M., Hibbert, A. M., & Robb, W. D. 1971, J. Phys. B: At. Mol. Opt. Phys., 4, 153
Burke, V. M., & Seaton, M. J. 1986, J. Phys. B: At. Mol. Opt. Phys., 19, L527
Eissner, W., & Nussbaumer, H. 1969, J. Phys. B: At. Mol. Opt. Phys., 2, 1028
Eissner, W., Jones, M., & Nussbaumer, H. 1974, Comput. Phys. Commun., 8, 270
Garstang, R. H. 1968, Ap&SS, 2, 336
Griffin, D. C., Badnell, N. R., & Pindzola, M. S. 1998, J. Phys. B: At. Mol. Opt. Phys., 31, 3713
Hansen, J. E., Raassen, A. J. J., & Uylings, H. M. 1984, ApJ, 277, 435
Hudgins, D., Herter, T., & Joyce, R. J. 1990, ApJ, 354, L57
Hummer, D. G., Berrington, K. A., Eissner, W., et al. 1993, A&A, 279, 298
Johnson, D. R. H., Barlow, M. J., Drew, J. E., & Brinks, E. 1992, MNRAS, 255, 261
Jones, M. 1970, J. Phys. B: At. Mol. Opt. Phys., 3, 1571
Jones, M. 1971, J. Phys. B: At. Mol. Opt. Phys., 4, 1422
NIST 2000, `http://www.nist.gov`
Sunderland, A. G., Noble, C. J., Burke, V. M., & Burke, P. G. 2002, Comput. Phys. Commun., 145, 311
Zeippen, C. J., Seaton, M. J., & Morton, D. C. 1977, MNRAS, 181, 527
Zhang, Y., & Liu, X.-W. 2002, MNRAS, 337, 499